A novel streamlined particle-unscented Kalman filtering method for the available energy prediction of lithium-ion batteries considering the time-varying temperature-current influence.

ZHANG, L., WANG, S., ZOU, C., FAN, Y., JIN, S. and FERNANDEZ, C.

2021

A novel streamlined particle-unscented Kalman filtering method for the available energy prediction of lithium-ion batteries considering the time-varying temperature-current influence

Liang Zhang[1,2] ID Shunli Wang[1,3] ID Chuanyun Zou[1] Yongcun Fan[1] Siyu Jin[3]

Carlos Fernandez[4]

[1]School of Information Engineering & Robot Technology Used for Special Environment Key Laboratory of Sichuan Province, Southwest University of Science and Technology, Mianyang, China

[2]School of Mechanical and Electrical Engineering, Mianyang Teachers' College, Mianyang, China

[3]Department of Energy Technology,Aalborg University, Aalborg East,Denmark

[4]School of Pharmacy and Life Sciences, Robert Gordon University, Aberdeen, UK

Correspondence
Shunli Wang, School of Information Engineering & Robot Technology Used for Special Environment Key Laboratory of Sichuan Province, Southwest University of Science and Technology, Mianyang 621010, China.
Email: 497420789@qq.com

Summary
Effective energy prediction is of great importance for the operational status monitoring of high-power lithium-ion battery packs. It should be embedded in the battery system performance evaluation, energy management, and safety protection. A new Streamlined Particle-Unscented Kalman Filtering method is proposed to predict the available energy of lithium-ion batteries, in which an Adaptive-Dual Unscented Transform treatment is conducted to realize the precise mathematical expression of its working conditions. For the accurate mathematical description purpose, an improved Synthetic-Electrical Equivalent Circuit modeling method is introduced into the internal effect equivalent process considering the influence of time-varying temperature and current conditions. As can be known from the experimental results, the proposed prediction method has a maximum estimation error of 2.27% and an average error of 0.80%, for the complex varying-current Beijing Bus Dynamic Stress Test. Under the Urban Dynamometer Driving Schedule working conditions, the available energy prediction has high accuracy with a maximum error of 1.83% and a voltage traction error of 3.28%. It provides vehicle-mounted available energy prediction schemes for effective management and safety protection of high-power lithium-ion batteries.

KEYWORDS
Available energy prediction: Lithium-ion battery: Streamlined particle-unscented Kalman filtering: Synthetic-electrical circuit modeling: Temperature current influence

INTRODUCTION

The available energy state of high-power lithium-ion battery packs is crucial to be predicted under different power supply applications. The technical bottleneck of its accurate prediction, energy status monitoring, and immature management has severely restricted the development of battery systems. The average circulating current has a great influence on the available energy status of lithium-ion batteries, which can be predicted by using Dual Extended Kalman Filtering, Gaussian Markov Modeling, and Unscented Particle Filtering algorithms.[1-3] The relaxation behavior of exotic lithium-ion batteries can be extracted to express its capacity decaying characteristics, including Dynamic Linear Modeling, Long Short-Term Memory (LSTM), Neural Network (NN), and Wide Operating Temperature Degradation methods.[4-8] Consequently, the robust adaptive Sliding Mode Observation algorithm is introduced into the effective and predictable correction stage as well as its diagnosis evaluation in advance.

To realize the accurate available energy prediction, observing strategies are introduced into the iterative calculation process, such as Adaptive Dual Kalman Filtering, Thermoelectric Coupling Modeling, and Open-Circuit Voltage (OCV).[9-12] In the calculation process, the effective energy state prediction can be realized by combining the experimental data. By conducting the State of Balance prediction for lithium-ion battery packs, the onboard dynamic balancing adjustment of the battery pack is carried out to improve its power supply performance. And then, Unscented Kalman Filtering (UKF), Equivalent Internal Resistance (EIR), Thermo-Dynamics, Gray Particle Filtering (GPF), and External Short Circuit methods[13-18] are used as proportional integral observers to realize the available energy prediction.

The Recurrent Neural Network illumination searching method is introduced to realize the available energy prediction, which is combined with Particle Filtering (PF) and other methods[19-22] to improve the residual energy prediction effect of lithium-ion batteries. The temperature compensation modeling strategies can be also considered to predict the energy state of the retractable charger. The Extended Kalman Filtering and Fractional Calculus Modeling strategies are combined for the cell-to-cell state prediction before its energy management.[23] The comparative analysis is performed entirely by introducing different ECM into the State of Charge (SOC) prediction process with delightful experimental results of battery cells.[24,25] The SOC and state of health can be predicted effectively by using built-in piezoelectric senors, actuators, and guided waves.[25] Using the backtracking search algorithm, the NN model can be established to express the energy state difference of the internal series cells, and the observation ability can be improved in exchange for shorter calculation time and accuracy. The constrained Bayesian Double Filtering method has a good effect on the available energy prediction of lithium-ion batteries effectively.[26] The prediction can be realized effectively by the embedded Square Root-Volume Kalman Filtering algorithm, which is adaptive to the time-varying power supply conditions of all climate batteries.[27] Intelligent Wavelet Neural Network and electro-thermal modeling strategies are constructed to achieve state prediction based on discrete wavelet transform.[28] The Dual Slip Mode Observer construction strategies are used to realize the combined available energy state prediction.[29] The observer can be designed by Grey Genetic Modeling, according to which loop-based iterative calculation process can be investigated. By measuring the internal resistance and constructing a multiscale dual H∞ filtering model combined with CKF and PF algorithms,[30] the capacity prediction effect can be verified. The remaining power state of the battery can be estimated through the current integration accumulation during the energy supply process. Since the confounding parameters are not considered, the Residual Energy State (RES) cannot be corrected by the surrounding temperature conditions. Subsequently, improved methods should be introduced to estimate the RES value and its real-time correction, including Reduction Pseudo Dimensional Modeling (RPDM), Gated Recursive-Unit NN, LSTM, CKF, and Fractional Order Modeling (FOM) algorithms.[31-35] As the single method still has shortcomings along with the economic growth rate change, which has a significant impact on the power state estimation and suitable to the permanent calculation. Subsequently, the high requirements for the initial value are limited to its application so that the results can be well applied in practice. For this reason, optimization methods such as GPF are introduced to solve this problem as well as the Gaussian Processing Regression and Deviation Compensation-Recursive Least Squares algorithms.[36-39] The

KF-based algorithm also provides an effective method to predict the energy state of the battery based on past state records. As the battery operating characteristics are nonlinear in most cases, the modeling accuracy should be considered when using composite multidimensional features and NN models,[40] which is the core reason why it is limited by environmental variables such as temperature and so on.

The treatment of discharging time and current is conducted with direct state calculation to describe the charge-discharge effect with appropriate estimation accuracy. Since the OCV value cannot be measured online and takes a long-shelved time, it is not suitable for large-scale promotion. The joint energy state estimation can be realized by introducing the backpropagation algorithm,[41] according to which the prediction accuracy is improved effectively. Because the external environment and aging characteristics play an important role in its application process, the improved chaotic and genetic algorithms are introduced to determine the effective energy of the battery, and it is used for the battery state prediction, as well as the FOM and statistical data-driven methods.[42-45] In the phase change composite material that is suitable for lithium-ion battery systems, the adaptive energy state prediction is realized when considering the thermal influence.

As for the available battery energy state prediction, the improved Synthetic-Electrical Equivalent Circuit (S-EEC) modeling method is introduced into the internal effect equivalent process considering the influence of time-varying temperature and current conditions, according to which the accurate characterization is realized for high-power lithium-ion batteries. Subsequently, an improved Streamline Particle-Unscented Kalman Filtering (SP-UKF) model is constructed for the residual power state prediction, which is encapsulated in a sub-module combined with effective feedback correction. The main evaluation factors are determined and its mathematical description is realized together with the theoretical analysis. The energy state is predicted effectively for lithium-ion batteries under varying Beijing Bus Dynamic Stress Test (BBDST) and Urban Dynamometer Driving Schedule (UDDS) working conditions.

MATHEMATICAL ANALYSIS

This section provides a detailed mathematical description method of the lithium-ion battery pack that is used for its onboard available energy prediction, which plays a positive role in promoting its power supply application.

Mathematical state-space description

An improved S-EEC model overcomes the defect that the traditional model cannot reflect steady-state voltage changes, which is adaptive to the nonlinear battery system with multiple advantages. By describing the internal battery as part 1 and the external load as part 2, the improved S-EEC construction strategy is designed and realized for high-power lithium-ion battery packs, as shown in Figure 1.

In Figure 1, the physical meaning of the main parameters in the S-EEC model can be expressed as shown in Table 1.

Subsequently, the internal reaction process of lithium-ion battery packs can be described accurately by considering the cell-to-cell difference in its packing power supply process, which simplifies the comprehensive modeling processes greatly. According to Kirchhoff's voltage law, the relationship between these model parameters can be obtained as shown in Equation (1).
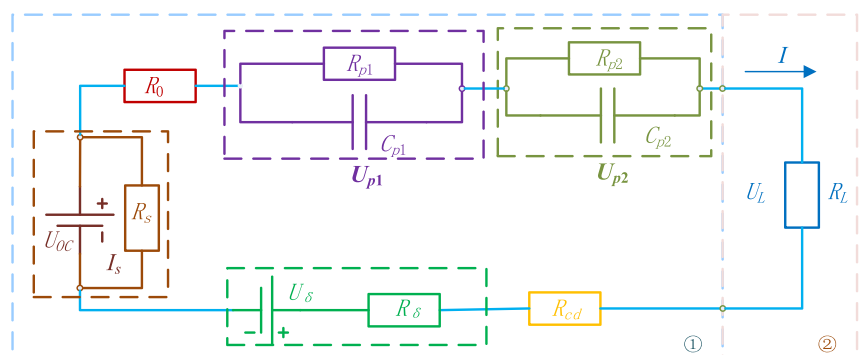

FIGURE 1 Synthetic-electrical equivalent circuit modeling

TABLE 1 Physical meaning of the main parameters in the synthetic-electrical equivalent circuit model

Parameters	Physical meaning
U_{OC}	Open circuit voltage
R_s	Self-discharge Resistance
I_s	Flowing current through the self-discharge resistance
R_0	Internal resistance
R_{p1}	First-order polarization resistance
C_{p1}	First-order polarization capacitance
U_{p1}	Voltage of the first-order parallel resistance-capacitance circuit
R_{p2}	Second-order polarization resistance
C_{p2}	Second-order polarization capacitance
U_{p2}	Voltage of the second-order parallel resistance- capacitance circuit
I	Total current
U_δ	Reverse Voltage for the Consistency Effect of the Connected Battery Cells
R_δ	Consistency of Influencing Resistance
R_{cd}	Differential Charge–discharge Resistance
U_L	Closed-circuit Voltage
R_L	Load Resistance

$$U_L(k) = (U_{\mathrm{OC}} - U_\delta) - (R_0 + R_\delta) * I(k)$$
$$- I(k)R_{p1}\left(1 - e^{-T_{s1}/(R_{p1}C_{p1})}\right)$$
$$- I(k)R_{p2}\left(1 - e^{-T_{s2}/(R_{p2}C_{p2})}\right) - I(k)R_{\mathrm{cd}}, \qquad (1)$$

wherein R_{p1} is the first-order polarization resistance and C_{p1} is the polarization capacitance, according to which T_{s1} can be obtained and used as its time constant. R_{p2} is the second-order polarization resistance and C_{p2} is the capacitance. And then, T_{s2} is used as its time constant. Since the model structure is not complicated, the iterative calculation amount is optimized effectively. Thus, the equivalent modeling convergence is realized quickly. In the proposed equivalent model, the discharge direction is positive, and the voltage across the polarization resistance increases along with the current rising process. Subsequently, the special time-domain relationship can be obtained as a supplement to the iterative calculation as shown in Equation (2).

$$\begin{cases} C_p dU_p/dt = I - U_p/R_p; R_0 = [(U_1 - U_2) + (U_4 - U_3)]/(2I) \\ U_5(k) = U_{\mathrm{OC}} - U_{p1}(k) - U_{p2}(k) = U_{\mathrm{OC}} - IR_{p1}e^{-T_{s1}/(R_{p1}C_{p1})} \end{cases}$$
$$- \quad IR_{p2}e^{-T_{s2}(R_{p2}C_{p2})}. \tag{2}$$

wherein Cp is the polarization capacitance. Up represents the terminal voltage of the parallel resistance-capacitance circuit. The total current is represented by I. The polarization resistance is represented by R_p and R_0 is the internal resistance of the battery. U_1 represents the voltage at the start time point of the pulse-current discharging process. U_2 represents the voltage at its stable time point. U_3 represents the voltage at the start time of pulse-current charging. U_4 represents the voltage at the time point when it is stable. U_5 represents the stable Closed-Circuit Voltage (CCV). The model parameters can be identified accordingly, which are used to replace the battery voltage change equation along with time extension, and the coefficients are used to describe its functional relationship. The calculation process is shown in Equation (3).

$$\begin{cases} y = c_1 - c_2 e^{-c_3 k} - c_4 e^{-c_5 k} \\ U_{OC} = c_1; R_{p1} = c_2/I; R_{p2} = c_4/I; C_{p1} = I/(c_2 c_3); C_{p2} = I/(c_4 c_5) \end{cases}$$

$$(3)$$

wherein y represents the functional output. k represents the discrete-time variable. Functional coefficient parameters are described by the coefficients of c_1, c_2, c_3, c_4, and c_5. Therefore, the model parameter values are calculated accordingly, named as R_{p1}, R_{P2}, C_{P1}, C_{P2}, and U_{OC}. Compared with other methods, it only needs to perform mixed pulse Constant Current (CC)-Constant Voltage (CV) treatment. The state-space equation of the equivalent model can be obtained, and the relationship between these parameters can be summarized as shown in Equation (4).

$$\begin{cases} S(k|k-1) = S(k-1) - \eta_I \eta_T I(k) T_s/Q_n - I_s(k) * T_s/Q_n \\ U_L(k) = (U_{OC} - U_\delta) - (R_o + R_\delta) * I(k) - I(k) R_{p1}\left(1 - e^{-T_{s1}/(R_{p1}C_{p1})}\right) \end{cases}$$

$$-I(k) R_{p2}\left(1 - e^{-T_{s2}/(R_{p2}C_{p2})}\right) - I(k) R_{cd}. \qquad (4)$$

wherein $S(k|k^{-1})$ represents the predicted value of available energy at the time point k obtained from the time point k-1. S(k-1) represents the available energy value at the time point k-1. η_I represents the efficiency coefficient affected by the current rate. η_T represents the efficiency coefficient affected by temperature. T_s represents the sampling time interval. Q_n is the rated battery capacity. The other parameters in the second part of Equation (4) are the same as those of Equation (1). In the instant charge-discharge process, the battery voltage change is recorded, and the internal parameters of the battery model are obtained by using Ohm's law and its time-domain relationship. Through tests under various working conditions, the internal resistance can be obtained accurately. The battery voltage change can be described under different effective energy levels and depth of discharge conditions, effectively reflecting its dynamic characteristics in the charge-discharge process. Consequently, the model parameters are obtained from continuous tests, in which the ohm resistance value can be calculated by analyzing the dynamic changes of the terminal voltage at the start and end time points. Meanwhile, the polarization resistance can be obtained by the slow change of the battery terminal voltage after a certain period as well as the polarization capacitance.

Adaptive unscented transformation

An improved Adaptive Dual-Unscented Transformation (A-DUT) strategy is proposed with high stability and feedback correction. Afterward, by calculating nonlinear variables, multivariate values can be obtained with the same statistical properties. Corresponding finite sampling points are chosen through state variable characteristics.

Then, the probability distribution characteristics of these specific data points are similar to the known variables. Using the symmetric strategy, the sampling points are obtained as x_i (i = 0, 1, 2, ..., 2n), the counting number of which is 2n + 1. Using the combination of the average covariance of y and P_y, the relationship between the state parameter and the observed variable can be obtained, and the expected accuracy is maintained through weighted calculation. The specific steps of A-DUT pro-vide more clues to the inner state plumbing of lithium-ion batteries. Afterward, the sigma points and corresponding weights are initialized by Equation (5).

$$x^i = \begin{cases} \hat{x}, i=0 \\ \hat{x} + \left(\sqrt{(n+\lambda)P_x}\right)_i, i=1...n \\ \hat{x} - \left(\sqrt{(n+\lambda)P_x}\right)_{i-n}, i=n+1...2n \end{cases} \qquad (5)$$

where n represents the state variable dimensionality. The sampling strategy in A-DUT has a serious impact on the estimation effect, and the symmetrical sampling strategy is adopted, which is convenient for calculation with good effect. The sampling points are converted into 2n+ 1 data points, which have the same mean and variance value as its original data. Each point has its corresponding mean and variance weight coefficients to resist the surrounding noise influence. The weight coeffi-cient considering the calculation influence is initialized according to Equation (6).

$$\begin{cases} \omega_m{}^0 = \lambda/(n+\lambda); \omega_c{}^0 = \lambda/(n+\lambda)+1-\alpha^2+\beta \\ \omega_m{}^i = \omega_c{}^i = 1/2*(n+\lambda), i=1...2n \end{cases}, \qquad (6)$$

where α represents the scattering factor degree, and the choice of α determines the closeness of the sampling points to its mean value, which is set as a positive num-ber from 0 to 1. For Gaussian distribution, the optimal redistribution factor is β = 2. k is an auxiliary scale factor that satisfies k + n ≠ 0. λ is a scaling parameter calculated by λ = α2(n + k)-n. By constructing a Sliding Coeffi-cient Window, reasonable adjustment of α and k improves the estimation accuracy. The dimension of the state variable x is initialed as n, and Px is set to be its average covariance matrix. Meanwhile, the observation variable is characterized by y, according to which the relational state variable expression is realized. The observation variable can be described by y = f(x), and the nonlinear transformation of the sigma point set is conducted accordingly as shown in Equation (7).

$$\begin{cases} \hat{y} = \dfrac{1}{2}\sum_{i=0}^{2n} \omega_m{}^i y_i = \dfrac{1}{2}\sum_{i=0}^{2n} \omega_m{}^i f(x_i) \\ P_y = \sum_{i=0}^{2n} \omega_c{}^i (y^i-\hat{y})(y^i-\hat{y})^T = \sum_{i=0}^{2n} \omega_c{}^i [f(x_i)-\hat{y}][f(x_i)-\hat{y}]^T \end{cases}. \qquad (7)$$

The goal of the A-DUT is to construct a certain number of sigma points together with the corresponding weights, ensuring the characteristic distribution of the nonlinear variables and approximating the performance index as much as possible. Then, the mean and covariance of y are calculated accordingly. According to the proposed modeling method, a single one-dimensional available energy state estimation model is established. Therefore, the terminal voltage U_L is set as the observed variable entangled by the measurement noise. Compared with other methods, the three-dimensional reduction is conducted in only one dimension. In this way, it reduces the computational time in the varying parameter correction by initializing $[S, U_{p1}, U_{p2}]^T$ as the state variables. Taking the discharging direction as positive, the state-space equation can be established as shown in Equation (8).

$$\begin{cases} S_k = S_{k-1} - (\eta_k T_s/Q_n)I_{k-1} + w_{k-1} \\ U_{L,k} = U_{oc}(S_k) - R_o I_{k-1} - R_{p1}\left(1-e^{-T_s/(R_{p1}C_{p1})}\right)I_{k-1} \\ \qquad - R_{p2}\left(1-e^{-T_s/(R_{p2}C_{p2})}\right)I_{k-1} + v_k. \end{cases} \qquad (8)$$

where Q_n is the rated battery capacity and T_s is the sampling time interval. Taking S_k as the state variable x_k, U_L can be obtained for the observation variable y_k that is conducted at the time point of k. The battery operating current I_k is used as the input variable u_k, so that the observation equation can be transformed into a typical nonlinear function.
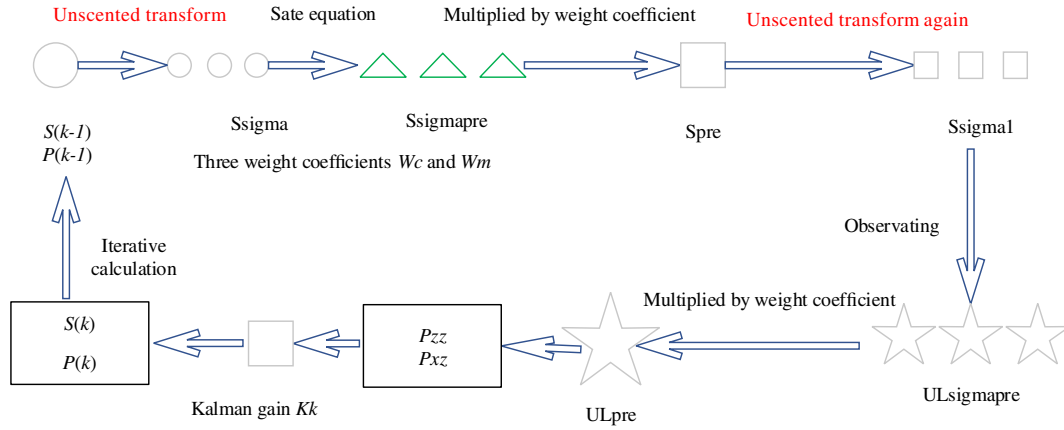

FIGURE 2 Available energy prediction flow chart of the Streamline Particle-Unscented Kalman Filtering method

Iterative prediction and correction

As a loop iterative calculation, the sigma point is selected according to the characteristic distribution of the referenced point, and the covariance of the sigma point x_k is guaranteed by the correction treatment. Then, these data points are introduced into the state equation to get the predicted data group. Using the generalized Kalman gain and combined with the difference of observed-predictor variables, the predictive value is corrected continuously to obtain the optimal value of the state variable. The iterative prediction-correction process of the SP-UKF method is shown in Figure 2.

Using the improved calculation thought, the specific energy state prediction is realized by conducting the previous initial parameter configuration. Corresponding research is carried out on this state prediction purpose, and the optimal state variable is obtained at the time point of k-1. Then, the A-DUT treatment is substituted to obtain the 2n + 1 sigma points for the state-space equation. Subsequently, one-step state variable prediction is realized, as shown in Equation (9).

$$\begin{cases} x_{k-1}^i = \hat{x}_{k-1}, i=0 \\ x_{k-1}^i = \hat{x}_{k-1} + \left(\sqrt{(n+\lambda)P_{k-1}}\right)_i, i=1,...n \\ x_{k-1}^i = \hat{x}_{k-1} - \left(\sqrt{(n+\lambda)P_{k-1}}\right)_{i-n}, i=n+1,...2n \end{cases} \quad . \quad (9)$$

After initializing the variables, the state value of each sampling period is predicted and updated for the available power estimation of the battery. Then, the Kalman gain is adjusted and the feedback error is corrected continuously according to the error covariance. As time accumulates, the loop-calculation number increases, and the available energy prediction value approaches the true value constantly, so it has self-correction characteristics in the estimation process. And then, the state variables are updated in time by the average weighting treatment, as shown in Equation (10).

$$\begin{cases} \hat{x}_{k|k-1} = \sum_{i=0}^{2n} \omega_m{}^i x^i{}_{k|k-1} = \sum_{i=0}^{2n} \omega_m{}^i f(x^i{}_{k-1}, u_{k-1}) \\ P_{x,k|k-1} = \sum_{i=0}^{2n} \omega_c{}^i \left[x^i{}_{k|k-1} - \hat{x}_{k|k-1}\right]\left[x^i{}_{k|k-1} - \hat{x}_{k|k-1}\right]^T + Q_k \end{cases}.$$

$$(10)$$

The parameter i represents the ith column of the covariance matrix. The average weight ω_m and variance weight ω_c are then obtained. After iterative calculation and verification, the parameters are initialized as k = 2, α = 0.01, and β = 2. And then, the state variable covariance is updated as shown in the second part of Equation (10). Even if the initial value is set to be far from the true value, the predicted value can approach the true value gradually as the algorithm proceeds with high estimation accuracy and strong robustness. Considering the observation noise statistics, the observation variable is updated by Equation (11).

$$\hat{y}_{k|k-1} = \sum_{i=0}^{2n} \omega_{mi} y^i{}_{k|k-1} = \sum_{i=0}^{2n} \omega_{mi} h\left(x^i{}_{k|k-1}, u_k\right). \qquad (11)$$

When the environment around the carrier changes, its statistical characteristics change greatly together with the observation noise of the carrier. Meanwhile, the prediction accuracy and stability are reduced greatly and the error covariance is updated, as shown in Equation (12).

$$\begin{cases} P_{yy,k} = \sum_{i=0}^{2n} \omega_c{}^i \left[y^i{}_{k|k-1} - \hat{y}_{k|k-1}\right]\left[y^i{}_{k|k-1} - \hat{y}_{k|k-1}\right]^T + R_k \\ P_{xy,k} = \sum_{i=0}^{2n} \omega_c{}^i \left[x^i{}_{k|k-1} - \hat{x}_{k|k-1}\right]\left[y^i{}_{k|k-1} - \hat{y}_{k|k-1}\right]^T \end{cases}.$$

$$(12)$$

The most computational operation is to recalculate the new sigma point set for each updating process of the SP-UKF iterative calculation method. In the correction stage, the square root of the error covariance is used to replace the error covariance of the state variables. Therefore, it transmits the square root value of the covariance directly, avoiding the decomposition in each loop calculation step. Through feedback correction, the influence of the surrounding environment is weakened, and the Kalman gain is updated according to Equation (13).

$$K_k = \frac{P_{xy,k}}{P_{yy,k}} = \frac{\sum_{i=0}^{2n} \omega_c{}^i \left[x^i{}_{k|k-1} - \hat{x}_{k|k-1}\right]\left[y^i{}_{k|k-1} - \hat{y}_{k|k-1}\right]^T}{\sum_{i=0}^{2n} \omega_c{}^i \left[y^i{}_{k|k-1} - \hat{y}_{k|k-1}\right]\left[y^i{}_{k|k-1} - \hat{y}_{k|k-1}\right]^T + R_k}.$$

$$(13)$$

When the battery operating current changes sharply, it will encounter a negative covariance problem in the later stage. The covariance P_k of the state variable also changes, so it becomes negative in the Cholesky decomposition. Consequently, the matrix must be semi-deterministic, otherwise, the calculation process cannot continue and fails. The reason for this failure is the rounding error of the numerical calculation. Therefore, the proposed SP-UKF is derived by replacing the traditional covariance with the square root of the state variable covariance. Through the iterative operations, the positive semi-definiteness and stability of the state variable covariance matrix are guaranteed, and the visible divergence can be overcome effectively. And then, the state update purpose is achieved through the optimal covariance matrix and real-time voltage measurement processing, as shown in Equation (14).

$$\begin{cases} \hat{x}_{k|k} = \hat{x}_{k|k-1} + K_k \left(y_k - \hat{y}_{k|k-1} \right) \\ P_{x,k|k} = P_{x,k|k-1} - K_k P_{yy,k} K_k^T \end{cases} \quad (14)$$

It is an integral part of covariance square root processing, which is also a recursive update of full covariance. Wherein, S is the square root of the covariance matrix P, that is, $SS^T = P$. As long as $S \neq 0$, P is nonnegative. The proposed SP-UKF method uses three powerful linear algebra techniques, named QR decomposition, Cholesky factor updating, and effective least squares. The Cholesky decomposition is performed on the theorem states. If $P R_{n*n}$ is symmetric and positive definite, there is a unique lower triangular matrix $S R_{n*n}$. The results show that $SS^T = P$ holds the diagonal elements of the positive matrix S virtually, which is the Cholesky factor of P. If $A R_{m*n}(m > n)$, the decomposition of A can be expressed as $A = Q*R$, where Q is an m*m matrix and R is the m*n upper triangular matrix. The upper triangular part is the transposition of P. And then, the Cholesky factor is updated accordingly by using the function of S = chol(P), and its matrix decomposition is updated again via the mathematical correction treatment. Then, the update function of cholupdate() is used to realize the Cholesky decomposition, and the square root S is used to replace the original covariance P.

Square root initializing and updating
The proposed SP-UKF calculation process mainly includes four parts: initialization, sigma point acquisition, time update, and status update processing. The error covariance P_0 is use to determine the initial value of the state variable. S_0 is the Cholesky factor of the covariance P_0, and its initial value is determined as shown in Equation (15).

$$\begin{cases} \hat{x}_0 = E(x_0); P_0 = E\left[(x_0 - \hat{x}_0)(x_0 - \hat{x}_0)^T \right] \\ S_0 = \text{chol}\{P_0\} = \text{chol}\left\{ E\left[(x_0 - \hat{x}_0)(x_0 - \hat{x}_0)^T \right] \right\} \end{cases} \quad (15)$$

Through the responding analysis, the capacity and internal resistance can be predicted and characterized for energy management. Considering different working conditions, the vertical sigma point collection is performed, as shown in Equation (16).

$$\begin{cases} x^i_{k-1} = \hat{x}_{k-1}, i = 0 \\ x^i_{k-1} = \hat{x}_{k-1} + \sqrt{(n+\lambda)} S^i_{k-1}, i = 1...n \\ x^i_{k-1} = \hat{x}_{k-1} - \sqrt{(n+\lambda)} S^{i-n}_{k-1}, i = n+1...2n \end{cases} \quad (16)$$

S^i_k denotes the ith column of the state variable covariance performed at the time point of k, and the average weighting parameter ω_m is obtained by the iterate calculation together with the variance parameter ω_c. According to the input variable at k-1, it can be predicted by the state equation, as shown in Equation (17).

$$\hat{x}_{k|k-1} = \sum_{i=0}^{2n} \omega_m{}^i x^i{}_{k|k-1} = \sum_{i=0}^{2n} \omega_m{}^i f\left(x^i{}_{k-1|k-1}, u_{k-1} \right). \quad (17)$$

Then, the error covariance of the state change is decomposed by the one-step prediction of the sampling points. Therefore, the vehicle-mounted working state estimation is conducted to describe its working characteristics, as shown in Equation (18).

$$\begin{cases} S_{xk}{}^- = qr\left\{ \left[\sqrt{\omega_c{}^{1:2n}} \left(x_{k|k-1}{}^{1:2n} - \hat{x}_{k|k-1} \right), \sqrt{Q_k} \right] \right\} \\ S_{xk} = \text{cholupdate}\left\{ S_{xk}{}^-, \sqrt{abs(\omega_c{}^0)} \left(x_{k|k-1}{}^0 - \hat{x}_{k|k-1} \right), \text{sign}(\omega_c{}^0) \right\} \end{cases}$$
$$(18)$$

Considering that the values of α and k may cause ω_c^0 to be negative, the semi-definiteness of the matrix should be guaranteed. S_{xk} represents the square root update value of the error covariance for the state variable at the time point of k shown in the second part of Equation (18). According to the prediction result of the state variable, the one-step predictor is constructed from the high-speed observing equation, as shown in Equation (19).

$$\begin{cases} y^i_{k|k-1} = h\left(x^i_{k|k-1}, u_k\right); \hat{y}_{k|k-1} = \sum_{i=0}^{2n} \omega_m{}^i y^i_{k|k-1} \\ S_{yk}{}^- = qr\left\{ \left[\sqrt{\omega_c^{1:2n}}\left(y_{k|k-1}{}^{1:2n} - \hat{y}_{k|k-1}\right), \sqrt{R_k} \right] \right\} \\ S_{yk} = cholupdate\left\{ S_{yk}{}^-, \sqrt{abs(\omega_c^0)}\left(y_{k|k-1}{}^0 - \hat{y}_{k|k-1}\right), sign(\omega_c^0) \right\} \end{cases}, \tag{19}$$

wherein S_{yk} represents the square root update value of the error covariance for the observed variable at time point k, and the state updating treatment is also investigated at this point. Therefore, considering the battery efficiency, the optimal depth of discharge is obtained. The cross-covariance of state and observed variables can be described by Equation (20).

$$P_{xy,k} = \sum_{i=0}^{2n} \omega_c{}^i \left[x^i_{k|k-1} - \hat{x}_{k|k-1} \right] \left[y^i_{k|k-1} - \hat{y}_{k|k-1} \right]^T. \tag{20}$$

Here, its value directly affects the size of Kalman gain, so it is taken as an important factor for the iterative calculation. Its accuracy has a great influence on the energy estimation effect. Through mathematical processing, it can adapt to various situations, thereby improving the estimation accuracy. Its calculation process is shown in Equation (21).

$$\begin{aligned} K_k &= P_{xy,k}\left(S_{yk}S_{yk}{}^T\right)^{-1} \\ &= \sum_{i=0}^{2n} \omega_c{}^i \left[x^i_{k|k-1} - \hat{x}_{k|k-1} \right] \left[y^i_{k|k-1} - \hat{y}_{k|k-1} \right]^T \left(S_{yk}S_{yk}{}^T\right)^{-1}. \end{aligned} \tag{21}$$

The Cholesky decomposition is introduced to calculate the square root of the covariance matrix to initialize the model parameters. The propagated and updated Cholesky factor can form abrupt sigma points in subsequent iterations. The error covariance correction is used to describe the state variables, according to which the experimental measurement of y_k is performed at the time point k, as shown in Equation (22).

$$\begin{cases} \hat{x}_{k|k} = \hat{x}_{k|k-1} + K_k\left(y_k - \hat{y}_{k|k-1}\right) \\ S_k = cholupdate\left(S_{xk}{}^-, K_k S_{yk}, -1\right) \end{cases}. \tag{22}$$

As can be seen from the calculation process, the time update of the Cholesky factor $S_{xk}{}^-$ can be realized by the compound QR matrix decomposition. It contains the weighted propagation sigma points and the square root matrix of the process noise covariance. The subsequent Cholesky update is essential to reduce the process error. Using these two steps to replace the time update of Px,kjk-1, it overcomes the shortcomings of poor stability in traditional algorithms and ensures the semi-determinism of the covariance matrix.

Adaptive window-factor correction

When predicting the battery state, particle degradation is encountered. Also, considering the influence of temperature on capacity, the coefficient correction is conducted to improve the ampere-hour integration processing accuracy, as shown in Equation (23).

$$S(t) = S(t_0) - \int_0^t \eta I(t)/(L_t Q_n) dt, \qquad (23)$$

where L_t is the temperature coefficient, which is the ratio of industrial temperature capacity to its standard value. Q_n is the battery capacity. $I(t)$ is the charge-discharge current. $S(t)$ is the SOC value at the time point of t. The temperature variations influence the calculation and make the estimation ability decrease, leading to inaccurate prediction results. Therefore, this phenomenon is considered to improve the estimation accuracy. To improve prediction accuracy and reduce particle degradation, an approximate Bayesian filtering treatment is conducted by the Monte Carlo probability density function. The iterative calculation process is designed for the adaptive window-factor correction, as shown in Figure 3.

In Figure 3, the iterative calculation flowchart of the adaptive window-factor correction is described and the detailed expression can be described as follows.

1. Initialization. The prior probability is used to generate N initial particles and their weights, as shown in Equation (24).

$$p(x_0) \xrightarrow{N} \left\{ S_0^i \right\}_{i=1}^N, \left\{ q_0^i \right\}_{i=1}^N = 1/N. \qquad (24)$$

2. The cyclic calculation process is designed as follows.
3. Updating. According to the system correction equation with a priori probability sample, a detailed mathematical description of the lithium-ion battery pack is carried out for the onboard available energy prediction. Considering the promotion effect, the particle weight is obtained and updated at the next time point according to Equation (25).

$$\left\{ S_k^i \right\}_{i=1}^N \Rightarrow w_k^i = w_{k-1}^i p\left(U_{L(k)} \big| S_k^i\right) = w_{k-1}^i p\left[U_{L(k)} - h\left(S_k^i\right)\right],$$

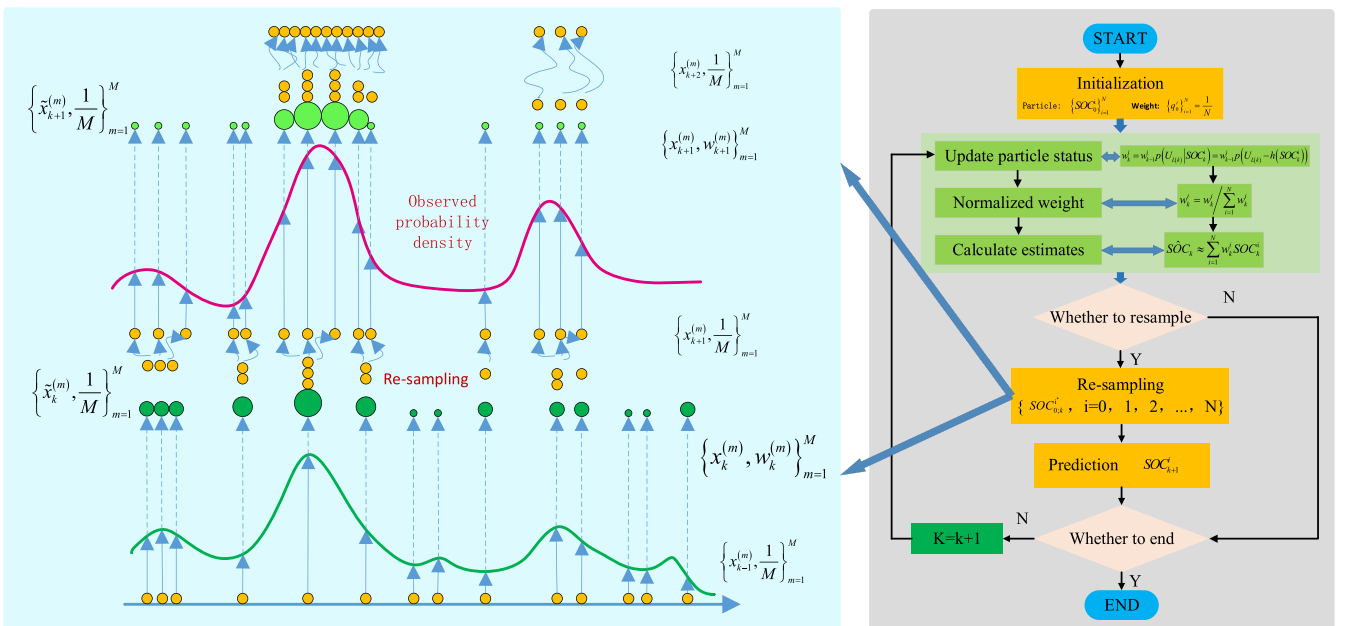$$i = 1, 2, \cdots, N. \qquad (25)$$

FIGURE 3 Iterative calculation process flowchart of the adaptive window-factor correction

4. Weighting normalization. The realization process mainly adopts the Bayesian criterion to weigh discrete random samples and complete the mean integral operation. The normalized weight is calculated according to Equation (26).

$$w_k^i = w_k^i \left/ \sum_{i=1}^{N} w_k^i \right. \qquad (26)$$

5. The average estimated value is calculated by Equation (27)

$$\hat{S}_k \approx \sum_{i=1}^{N} w_k^i S_k^i. \qquad (27)$$

6. Resampling. The effective particle number is calculated as shown in the first part of Equation (28).

By judging the difference in size, a new particle set is obtained, as shown in the second part of Equation (28).

$$N_{\text{eff}} = 1 \left/ \sum_{i=1}^{N} (w_k^i)^2 \right. \xrightarrow{N_{\text{eff}} \le N_s} \left\{ S_{0;\ k}^{i^*}, i = 0,1,2,\cdots,N \right\}. \qquad (28)$$

7. Prediction. The state equation is used to predict the unknown state parameter at the time point of k + 1.
8. The end condition is determined for the iterative calculation program. If it is not over, the time point is set as k = k + 1 and the procedure turns to step 1).

When it is used to estimate the battery state under complex working conditions, the processing noise affects its influence on the state-space expression established by the observing calculation. When setting the model boundary, the observed variable is equal to the load voltage considering the state variable change, as shown in Equation (29).

$$\begin{cases} x_{k+1} = f(x_k, i_k, w_k) = x_k - (ni_k \Delta t)/(\eta_i \eta_T \eta_n Q_n) + w_k \\ y_{k+1} = f(y_k, i_k, w_k) = k_0 - Ri_k - k_1/x_k - k_2 x_k + k_3 \ln(x_k) \end{cases}$$
$$+ k_4 \ln(1 - x_k) + v_k. \qquad (29)$$

where w_k is processing noise and v_k is observation noise, which obeys the functional relationship of $w_k \sim N(0, Q)$ and $v_k \sim N(0, R)$. Δt is the sampling period. When calculating the innovation covariance matrix, it is necessary to perform the window averaging on the sampling values of the innovation sequence to overcome unsatisfactory results. There is a problem in choosing the window function and size unless it is coordinated. If the function window width is too small, the predicted covariance matrix has greater noise. On the contrary, the covariance matrix reflects large characteristics. The window size of M is initialized from 1tok.When M = 1, it has the worst effect with a small calculation amount. When M = k, it works well, but the calculation amount becomes larger. The window size is set as M = 3 artificially with a good prediction effect. The relevant covariance matrix is described by defining the unit innovation, and its calculation process is shown in Equation (30).

$$E_k = E\left(e_k e_k^T\right) = P_{yy,k}$$
$$= \sum_{i=0}^{2n} \omega_c^i \left[y_{k|k-1}^i - \hat{y}_{k|k-1} \right] \left[y_{k|k-1}^i - \hat{y}_{k|k-1} \right]^T + R_k. \qquad (30)$$

On this basis, a unique adaptive window factor d is defined dynamically to determine the window size. It has the advantages of high judgment efficiency and fast convergence speed, which is suitable for real-time forecasting. Considering the prediction effect and the calculation amount comprehensively, the two factors can reach an appropriate balance when the statistical characteristics of the measurement noise are not clear. After that, the forecast deviation is avoided effectively and the forecast result is accurate. The adaptive window factor d represents the measured value, and the expression is shown in Equation (31).

$$
\begin{aligned}
d &= e_k{}^T E_k{}^{-1} e_k \\
&= e_k{}^T \left\{ \sum_{i=0}^{2n} \omega_c{}^i \left[y^i{}_{k|k-1} - \hat{y}_{k|k-1} \right] \left[y^i{}_{k|k-1} - \hat{y}_{k|k-1} \right]^T + R_k \right\}^{-1} e_k,
\end{aligned}
$$

$$(31)$$

where the function of d is to adjust the width of the adaptive window M dynamically. When the innovative correlation matrix is large, its calculated value is less than 0. The predicted value differs from the measured value greatly. The window opening width increases until the terminal point, making the predicted value closer to the true value, $M = k$. When the innovation correlation matrix is small and the calculated d is greater than 1, the predicted value is better with no tedious calculation requirement. The window is simplified as $M = 1$ to realize the accurate calculation. When $0 < d < 1$, $M = k \times \eta^{d-\mu min}$ takes an appropriate value. The uncertain size of the adaptive window M is shown in Equation (32).

$$
\begin{cases}
M = 1, d \geq \mu_{max}; M = k, d \leq \mu_{min} \\
M = k \times \eta^{d - \mu_{min}}, \mu_{min} < d < \mu_{max}
\end{cases},
\qquad (32)
$$

where μ_{min} and μ_{max} are the determination thresholds. According to experience, they are initialed as $\mu_{min} = 0$ and $\mu_{max} = 1$. η represents the convergence rate of the window M that is smaller than 1. Since k represents the target time point, the adaptive window length varies from 1 to k. Consequently, an improved adaptive noise covariance matching method is introduced and applied for effective energy estimation, according to which the accuracy is improved greatly. The numerical instability and nonpositive problems are introduced in detail, which improves the modeling accuracy by covariance matching.

EXPERIMENTAL ANALYSIS

Test procedure design

Lithium-ion cobalt oxide batteries have the advantages of high energy density and large volume density, which have been promoted and applied initially in the power supply fields such as airplanes.[28] For the related onboard available energy prediction, the constructed management system uses a temperature box to maintain a hypothetical environment. According to the embedded signal data, the relationship between voltage changes under different current rates is analyzed to predict the available energy. Considering the application performance requirements, real-time status monitoring is carried out as well as its remaining energy prediction. The running status measurement subsystem is designed and a management system is constructed, which uses special semiconductors to perform real-time voltage detection. In this experiment, lithium cobalt oxide batteries are selected as the experimental object, and the platform is constructed as shown in Figure 4.

The battery experimental charge-discharge platform is constructed by the high-rate power battery charge-discharge tester (CT-4016-5 V100A-NTFA). The incubator is a three-layer independent high-low-temperature test (DGBELL BTT-331 C). Subsequently, the experiment is carried out at different temperature conditions. An effective energy evaluation mechanism is established to ensure the application safety of energy storage and power supply systems. Compared with the traditional management system, the electronic load is used for discharging maintenance, and the real-time protection unit is also designed to reform the charge-discharge process in real-time.

Model parameter identification

The identification steps are designed as follows. (1) The batteries are charged and discharged three times using a current rate of 0.20 C until the terminal voltage of 4.15 V is reached. After that, it is discharged to a cutoff voltage of 3.00 V at 0.10 C. After 12 hours of full charge-discharg treatment, the battery is activated. (2)
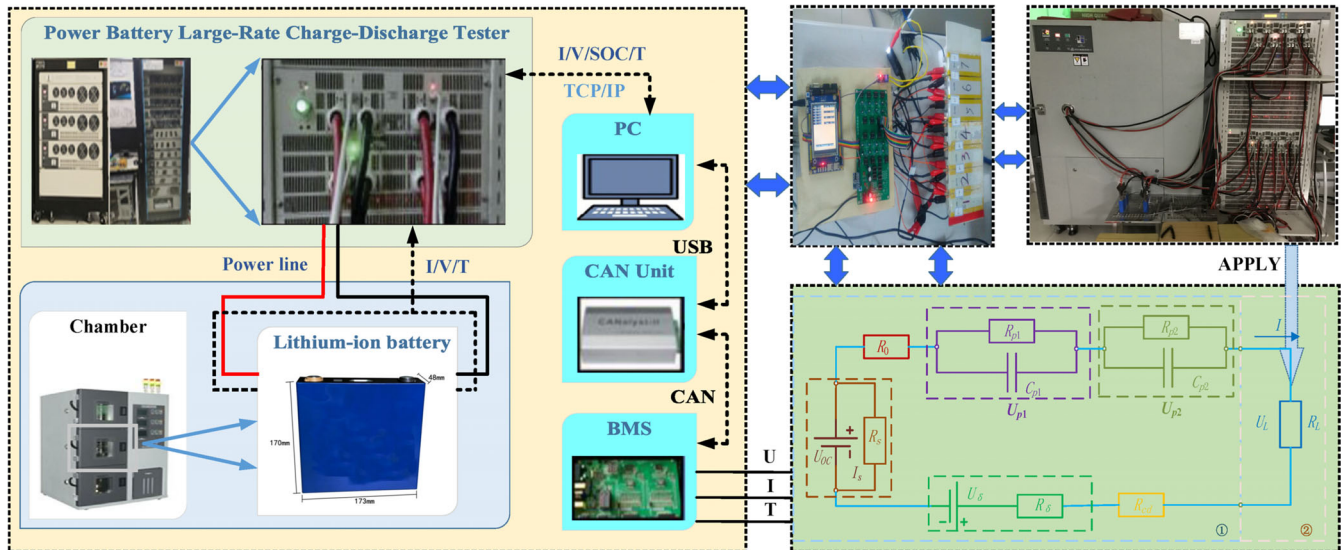

FIGURE 4   The experimental platform design and application

The charging operation is performed by the CC charging with a current rate of 1/3 C until the voltage reaches the cutoff value of 4.20 V. It is then continued to be charged by using the constant voltage of 4.20 V until the charging current rate reduces to be 0.05 C. At this time point, the battery is considered to be charged fully and remains shelved for 1 hour to stabilize the voltage and temperature. (3) It is pulse-discharged by constant-current discharging of 1 C for 10 seconds, and then a 40 seconds break is imposed. The battery is pulse-charged for a duration of 10 seconds by using the CC maintenance of 1 C. After the charging process is stopped, it is shelved for 40 seconds. And then, a completed cycling experiment throughout the overall discharging maintenance is completed according to the designed test procedure.(4) The battery is discharged at a current rate of 1.00 C for 3 minutes (SOC = 0.95) and shelved for 40 minutes. Consequently, the experiment is performed, in which the real-time parameters are recorded in real-time, including OCV, discharging current, discharging time, and so on. (5) Steps of (3) and (4) are repeated by and the experiments are performed at different SOC levels, respectively. (6) After performing the complete experiment, the battery is discharged with a 1 C current rate for 3 minutes to reduce the available energy value by 5.00%. After the discharge, the battery is set to stand for 1 hour, and then the next cycling experiment is performed and introduced into the whole discharging process until the available energy drops to zero.

The effect of reverse voltage for serially connected cells is engaged in the iterative calculation process, so its parameter value is not necessary to be identified as well as the self-discharge resistance. As the self-discharge process is a slow variation procedure, it is characterized by the cycling number and the periodic measurement. Taking U1 as the battery terminal voltage, it is conducted at the time point when the discharge starts to be investigated. U2 is the voltage when the discharge starts for 3 seconds. U3 is the terminal voltage of the time point when the discharge maintenance is finished, and its dis-charging time interval is 10 seconds. U4 indicates the ter-minal voltage of its ending time point in the pulse discharging maintenance. After the terminal voltage rises instantaneously for about 40 seconds, U_5, is measured to start the charging step at the

end of the holding time interval. To achieve effective parameter representation, the polynomial fitting method is introduced for the functional expression, and the coefficients of each power term are obtained for subsequent calculations. After substituting 10 groups of voltage data onto SOC from 1 to 0.1, the parameters of C_1, C_2, C_3, C_4, and C_5 are obtained as shown in Table 2.

According to the experimental data onto each SOC level point, the S-EEC parameter values are obtained corresponding to the time-varying process. The parameter values of the circuit components are obtained by substituting these parameters into the calculation process as shown in Table 3.

As can be seen from the experimental results, R_0 increases slowly along with the SOC decrease, and the variation ranges are small toward the slow change rate. R_p reduces slowly along with the SOC decrease but increases sharply when it is lower than 0.15 due to the acceleration. After the curve fitting of all the parameters, the coefficients can be obtained as shown in Table 4.

TABLE 2   Model parameters corresponding to different state of charge (SOC) levels

SOC	C_1	C_2	C_3	C_4	C_5
1.0	4.170590	0.011250	0.098340	0.002280	159.995950
0.9	4.041601	0.014079	0.097746	0.004008	159.996649
0.8	3.929558	0.014736	0.095591	0.003690	159.996882
0.7	3.827812	0.014795	0.093477	0.003617	159.996785
0.6	3.712430	0.010960	0.093045	0.002304	159.996889
0.5	3.646312	0.010340	0.080770	0.002230	159.996773
0.4	3.608898	0.010201	0.087310	0.002044	159.996670
0.3	3.573331	0.010223	0.084905	0.003043	159.997091
0.2	3.499115	0.011859	0.095551	0.003696	159.993569
0.1	3.414992	0.021863	0.112778	0.012579	159.999451

TABLE 3   Model parameters corresponding to different state of charge (SOC) levels

SOC	R_0	U_{oc}	R_{p1}	R_{p2}	C_{p1}	C_{p2}
1.0	0.003922	4.17059	0.000225	4.56525E-05	45 189.95	136.9073
0.9	0.004101	4.0416014	0.000282	8.01674E-05	36 333.6	77.96353
0.8	0.004083	3.9295585	0.000295	7.38069E-05	35 496.17	84.68205
0.7	0.004068	3.8278124	0.000296	7.2348E-05	36 153.47	86.38972
0.6	0.00407	3.7124298	0.000219	4.60785E-05	49 028.56	135.6408
0.5	0.004083	3.6463121	0.000207	4.45968E-05	59 867.7	140.1475
0.4	0.004099	3.6088983	0.000204	4.08835E-05	56 137.49	152.8764
0.3	0.004126	3.5733311	0.000204	6.0866E-05	57 603.74	102.6865
0.2	0.004179	3.4991152	0.000237	7.39157E-05	44 123.88	84.55922
0.1	0.004318	3.4149921	0.000437	0.000251584	20 279	24.84268

TABLE 4 Model parameters corresponding to different state of charge levels

Coefficients	R_0	U_{oc}	R_{p1}	R_{p2}	C_{p1}	C_{p2}
Intercept	0.00452	3.47947	0.00123	8.81E-04	−41 727.647	−97.4336
B1	−0.00216	−2.51901	−0.01324	−0.01032	955 306.591	1948.584
B2	−0.00162	26.91376	0.07012	0.05177	−4.42E+06	−9844.81
B3	0.03312	−97.2463	−0.19162	−0.13285	1.24E+07	31 964.77
B4	−0.08614	166.1953	0.28091	0.18228	−2.03E+07	−55 554.0
B5	0.09037	−133.4920	−0.20715	−0.12626	1.66E+07	45 574.78
B6	−0.03417	40.83975	0.05998	0.03455	−5.21E+06	−13 855.9

After being shelved for a long time, the polarization effect and ohm resistance influence are reduced greatly. The measured terminal voltage equals the OCV value toward the electromotive force E. The terminal voltage drops rapidly from SOC = 1.00 to 0.85, and the OCV decreases by 0.04 V to 0.06 V for every SOC level decrease. The OCV drop is stable within 0.03 V for every COP decrease when it enters a stable period between 0.85 and 0.15, and the voltage fluctuation is small. After the SOC is lower than 0.15, the OCV drops rapidly and the voltage fluctuates greatly as the battery discharges.

Temperature influence and correction

According to the correction target of the prediction process, the temperature influence of the battery capacity is analyzed as well as the current rate effect temperature conditions. Considering the temperature difference caused by the ground-to-high-altitude variation, the characteristics are obtained under different temperature conditions in the calculation process of the Coulomb efficiency coefficient ηT. The experimental analysis is carried out at different temperature conditions, which is conducted in the current rate range of (0.2, 0.4, 0.6, 0.8, and 1.0) and a widely varying temperature range temperature conditions (20.00, 10.00, 0.00, 10.00, 20.00, and 40.00 C). Then, the variation on temperature and the current rate is obtained for the experimental samples of the lithium-ion battery packs. The acquisition of the capacity is obtained by the discharging experiments from the full-charged state to the cut-off discharging voltage.

Besides, its total power is released fully in this manner, the discharge capacity law is obtained completely as shown in Figure 5.

As can be seen from different experimental conditions, the CC discharging current rate has a great influence on the capacity. When the ambient temperature is greater than 0°C, the current rate has little influence on the battery capacity when the C-rate is smaller than 5, but the discharging C-rate has a great influence on the capacity. However, when the experimental temperature is lower than 0°C, the capacity decreases corresponding to the discharging current rate increase. At low ambient temperature conditions, when the discharge rate is greater, the capacity becomes smaller. When the temperature is higher than 40.00°C, the discharge power decreases along with the temperature increase. Through the operating characteristic analysis over a wide temperature range, a suitable temperature range is established from 5.00 C to 35.00 C, and the optimal temperature range is obtained for the OCV characteristics as shown in Figure 6.
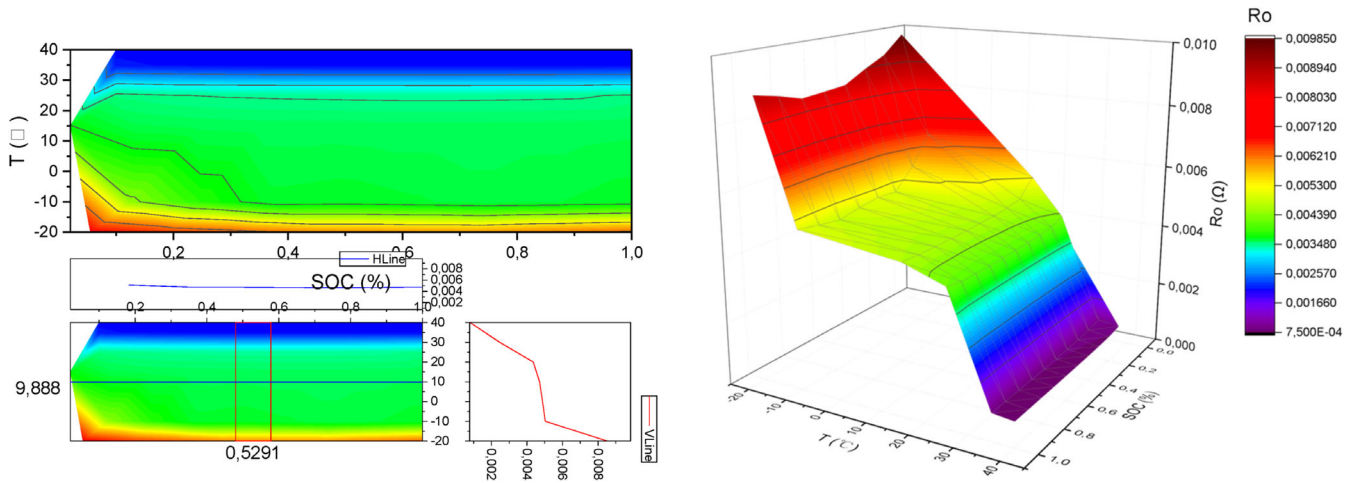
FIGURE 5 The battery internal resistance variation for different temperature conditions
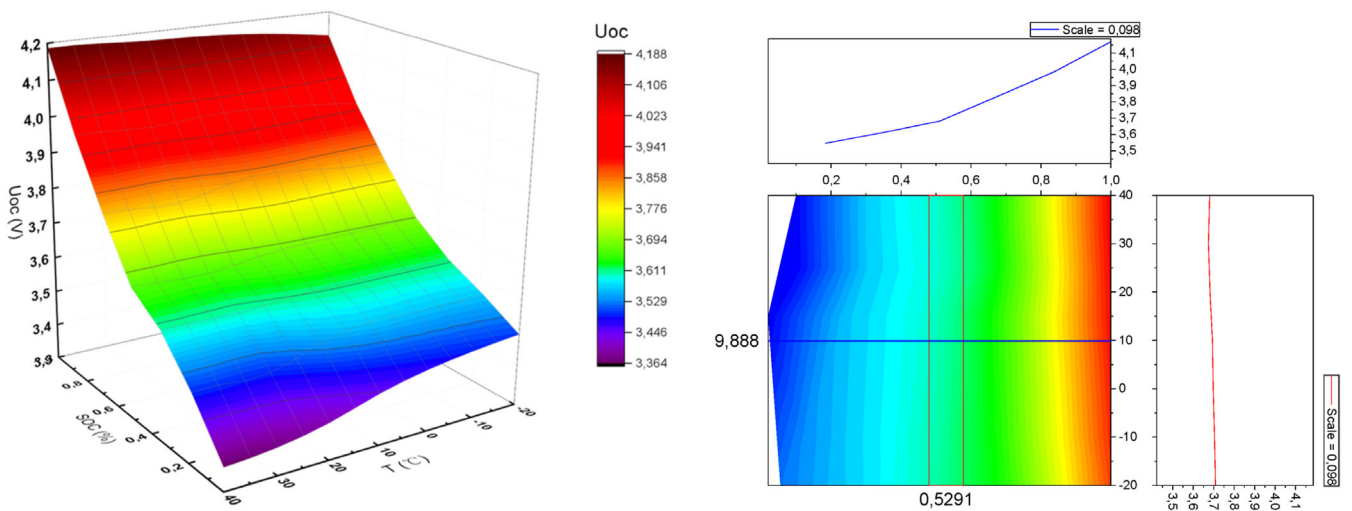

**FIGURE 6** The open-circuit voltage change corresponding to the temperature variation

Through the discharging experiment at different temperature conditions, the voltage changing law is obtained along with the temperature variation. As can be known from the experimental results, the voltage variation on different available energy levels can be divided into the following three stages together in the CC discharging process. In the first phase, the current drops in the initial discharging process at a low speed. In the second phase, the voltage enters the plateau after a certain discharging period and the descent rate slows down. In the third phase, the voltage enters a steep drop at the end of the discharging period when the SOC value is lower than 20%. The functional relationship is used to obtain its corresponding efficiency coefficient for different temperature conditions. Then, the experimental results are compared with the originally collected data to verify the tracking effect of the fitting curve, which shows that it has tougher characteristics than the traditional calculation methods.[46]
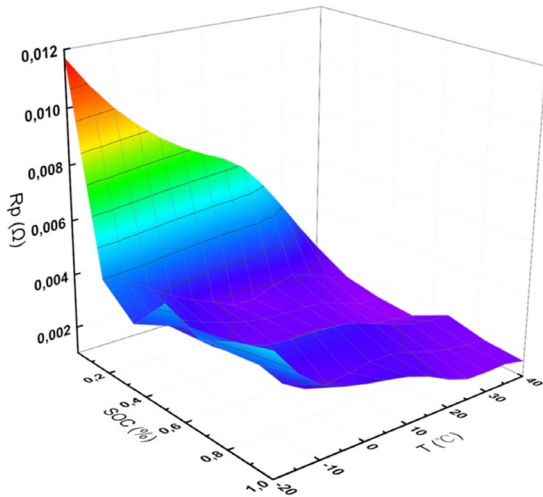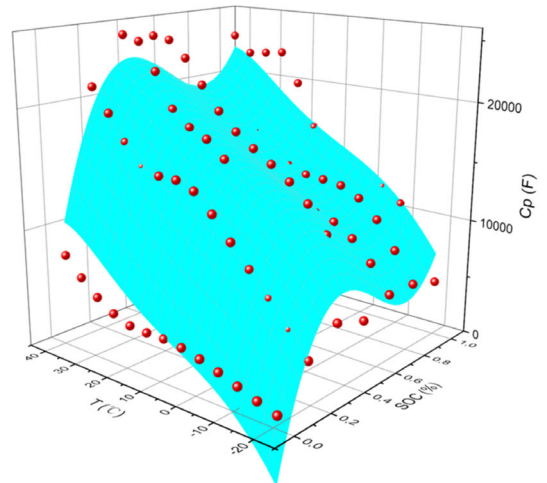
(A) Polarization resistance variation for varying SOC and T
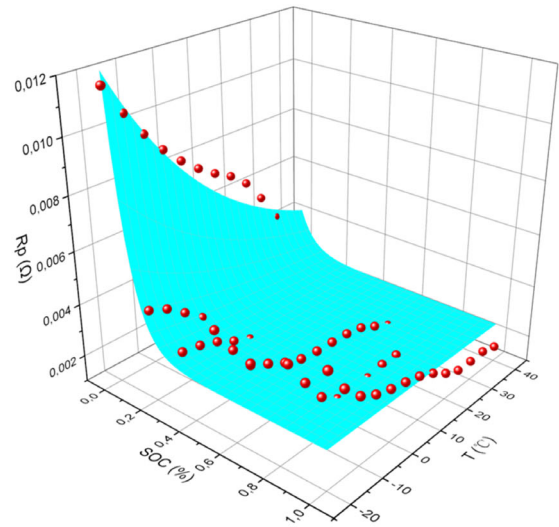
(B) Traction of the polarization resistance variation
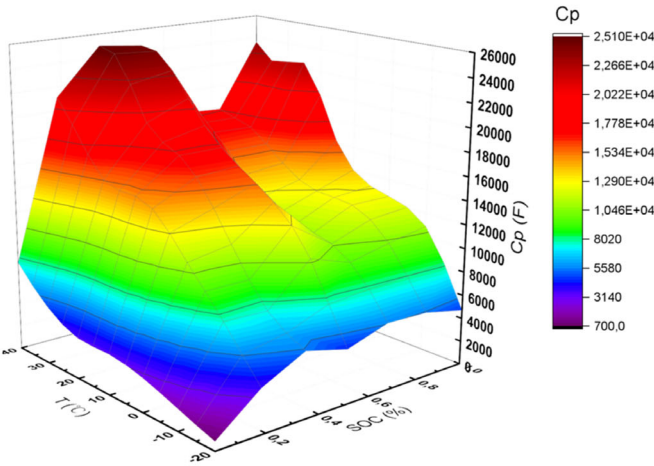
(C) Polarization capacitance variation for varying SOC and T

(D) Traction of the polarization capacitance variation

FIGURE 7 Polarization effect variation along with the state of charge and temperature change

Time-varying polarization effect

By comparing the charge-discharge curves at different temperature conditions, there is a certain CCV difference. When the SOC value is between 20.00% and 50.00% at 20.00 C, the charging voltage is nearly 0.06 V higher than the discharging voltage. This difference is mainly affected by the voltage drop of the internal resistance. When the SOC value is between 60.00% and 90.00%, the charging CCV value is 0.03 V higher than its discharging value. At the temperature condition of 10.00 C, it is 0.10 V higher than the discharging CCV value. When the value is 0, the CCV value is 3.00 V. When the value equals 100.00%, the terminal voltage of 4.15 V equals the cut-off charging voltage. The polarization resistance variation on the experimental temperature change is described as shown in Figure 7.

As can be known from Figure 7, the discharging current increases, and the terminal voltage shows a downward trend as the cycling number increases. The fitting equation has a good effect on the battery characteristic simulation, which is introduced into the subsequent iterative calculation process. Furthermore, the experimental analysis of the temperature variation is carried out with higher accuracy compared with the reference. According to the experimental data on different temperature conditions, the voltage variation curve is obtained during the charge-discharge period. During the charging process, it has a significant voltage change along with low-temperature conditions, but the voltage changes along with the available energy variation when the temperature increases.[47] The temperature monitoring module is placed in its management system via a heater plate and a sink to avoid the over-charge and over-discharge disks on low-temperature conditions together with its real-time correction. The capacity utilization increases the useful life in case of its high-temperature conditions, and the CCV changes similarly in temperature. The influencing effect of temperature variation on the critical point is significant. When the voltage equals 3.80 V, the valued battery available energy equals 60% at 40.00 C but equals 20% at -20.00 C.

Varying current RES prediction

To verify the applicability of the proposed SP-UKF prediction method lithium-ion batteries are used in the experiments. The prediction effect is analyzed when its initial value is small. The prior-knowledge-independent equalization is investigated to improve its uniformity with energy and efficiency, realizing the capacity prediction of the group working lithium-ion batteries. An available energy prediction model is conducted that is adaptive to the pulse-current driving patterns of electrical vehicles. By comparing the prediction results from the references, the experimental result of the proposed method has a better accuracy effect. The prediction algorithm is implemented in performing the pulse-current discharge maintenance. The BBDST working condition is used. The steps are organized accordingly and the experimental tests are conducted by the schedule shown in Table 5.

TABLE 5   Simulated working condition parameters and their step-by-step design

| P_h (kW)	P_c (W)	Single step (s)	Total (s)	Working conditions
37.5	69	21	21	Start
72.5	135	12	33	Accelerate
4.5	9	16	49	Sliding
−15	−27	6	55	Brake
37.5	69	21	76	Accelerate
4.5	9	16	92	Sliding
−15	−27	6	98	Brake
72.5	135	9	107	Accelerate
92.5	174	6	113	Rapid acceleration
37.5	69	21	134	Accelerate
4.5	9	16	150	Sliding
−15	−27	6	156	Brake
72.5	135	9	165	Accelerate
92.5	174	6	171	Rapid acceleration
37.5	69	21	192	Accelerate
4.5	9	16	208	Sliding
−35	−66	9	217	Brake
−15	−27	6	229	Brake
4.5	9	71	300	Parking

Wherein, P_h (kW) is the output power under the starting acceleration condition. Since the experiment is carried out on the battery cell, the data onto P_c (W) is obtained by reducing P_h (kW), which is used for the experimental test. The time of one complete experimental test is 300 seconds and the BBDST is performed 20 times for the battery, according to which the experimental result is obtained. To analyze the estimation effect of the proposed algorithm when the current is abrupt, a piecewise CC test is designed and compared with the references, in which the initial discharging current rate is 1 C. Thus, the battery operating current is mutated into 0.5 C after 20 minutes discharging maintenance, which is then changed into 0.3 C after 25 minutes discharging maintenance. The output voltage tracking effect of the time-varying current condition is shown in Figure 8.
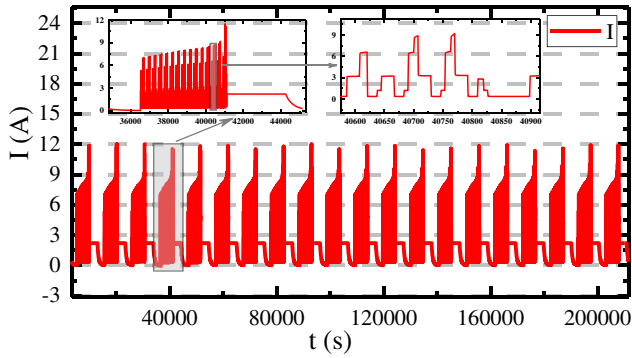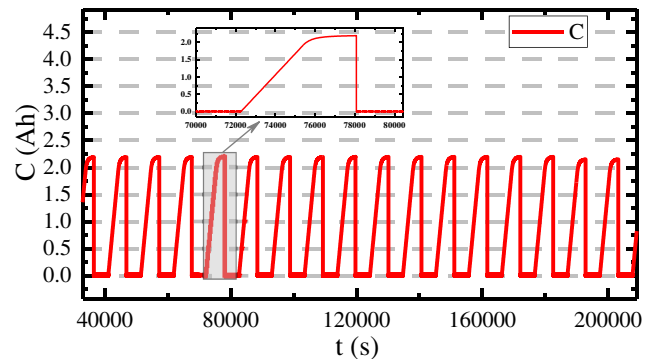

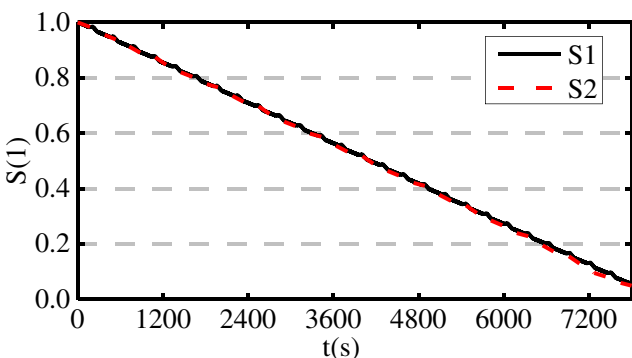(A) Current variation for the long-term test
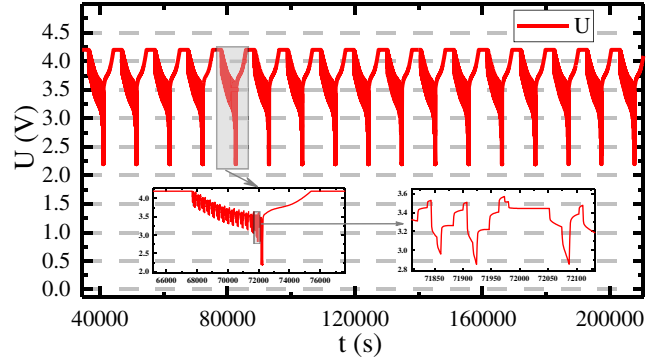
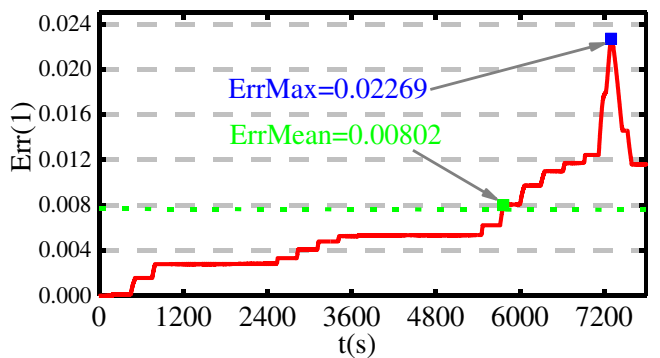(B) Corresponding CCV variation to the current change
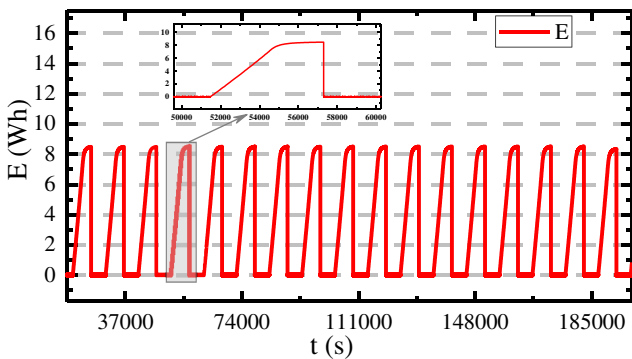
(C) Corresponding energy variation to the current change

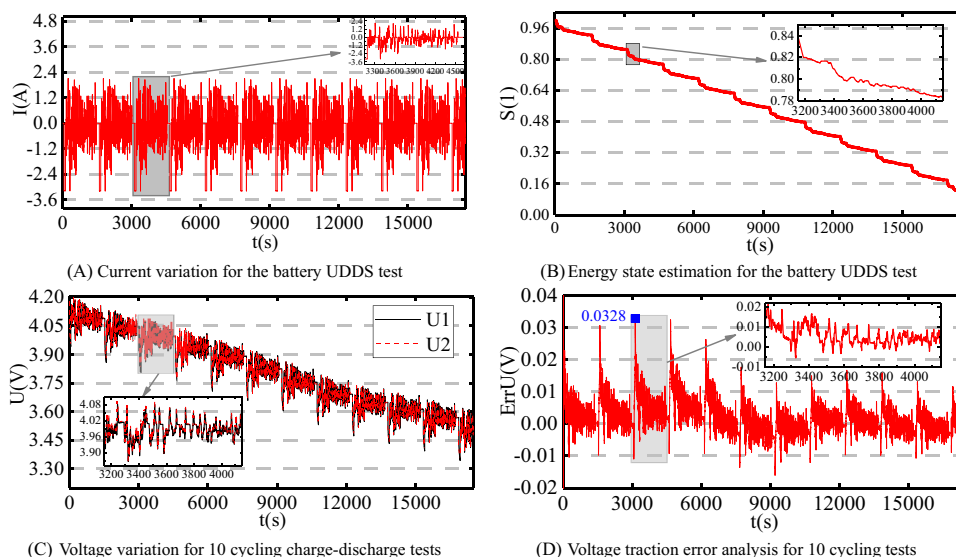(D) Corresponding capacity variation to the current change

(E) One cycle state estimation result and comparison

(F) One cycle state estimation error analysis

FIGURE 8   The experimental test under time-varying Beijing bus dynamic stress test current working conditions

FIGURE 9 The experimental results for the urban dynamometer driving schedule working conditions

(A) Current variation for the battery UDDS test

(B) Energy state estimation for the battery UDDS test

(C) Voltage variation for 10 cycling charge-discharge tests

(D) Voltage traction error analysis for 10 cycling tests

As can be known from the experimental results, the proposed algorithm has good prediction performance when the current is abrupt. It has strong convergence that approaches quickly to the theory less than 10 seconds. The maximum estimation error of this prediction algorithm is 2.27% and the mean error is 0.80% for the complex varying-current BBDST working conditions, which realizes the residual energy state estimation effectively. The UDDS working condition is then designed to verify its robust characteristics and the results can be obtained as shown in Figure 9.

As can be known from the experimental results, the proposed available energy prediction method has good accuracy for lithium-ion batteries under different working conditions. A comparative study is conducted for a three-model-based algorithm of estimating the battery available energy, which has high accuracy and low computational burden even with the extreme pulse-current charge-discharge working condition compared with the experimental results reported in References.[42, 43, 48] It has high accuracy with a maximum error of 1.83% and its maximum voltage traction error is 3.28% for the UDDS working conditions. The available energy prediction curve has a small variation and error value that can realize the state monitoring with high accuracy in its management system. The available energy prediction results are consistent with the technical reports,[49-52] in which it is diagnosed according to its surface temperature variation by correcting the actual initial value in the prediction process.

CONCLUSION

An improved SP-UKF method is proposed and introduced into the remaining power prediction process, which can obtain the available energy value accurately. Combined with the integrated available energy prediction method, it works well and realizes the onboard endurance capability monitoring effectively. Different current rates and temperature experiments are carried out, according to which the available energy prediction performance is validated by various working condition tests. For the complex varying-current BBDST working conditions, the proposed SP-UKF prediction algorithm has a maximum estimation error of 2.27% and an average error of 0.80%. Under UDDS working conditions, the available energy prediction method has high accuracy with a maximum estimation error of 1.83% and voltage traction error of 3.28%. As for the battery energy state estimation, it achieves an accurate available energy prediction, providing an effective method for the residual energy prediction of the high-power lithium-ion batteries. As the proposed prediction method is suitable for the online state estimation with high accuracy and low calculation amount requirement, more experimental tests will be conducted for its adaptive characteristic verification, so that its sub-module will be improved as well for real-time energy management.

NOMENCLATURE

$U_L(k)$	closed-circuit voltage
U_{OC}	open-circuit voltage
U_δ	consistency reverse voltage
R_0	battery internal resistance
$I(k)$	total current
R_{p1}	first-order polarization resistance
C_{p1}	first-order polarization capacitance
T_{s1}	first-order time constant
R_{p2}	second-order polarization resistance
C_{p2}	second-order polarization capacitance
T_{s2}	second-order time constant
R_{cd}	differential charge-discharge resistance
c_1 to c_5	functional-coefficient parameters
$S(k\text{-}1)$	available energy value at time point k-1
η_T	efficiency factor influenced by the temperature
Q_n	rated battery capacity
Cp	polarization capacitance
Up	terminal resistance-capacitance voltage
Rp	polarization resistance
$U1$	pulse discharging start time point voltage
$U2$	pulse discharging stable time point voltage
$U3$	pulse charging start time point voltage
$U4$	pulse charging stable time point voltage
$U5$	stable closed-circuit voltage
$Up1$	first-order resistance-capacitance voltage
$Up2$	second-order resistance-capacitance voltage
y	functional output
k	discrete-time point variable
S	predicted available energy at time point k from
$(k|k\text{-}1)$	k-1
ηI	efficiency factor influenced by the current rate
Ts	sampling time interval
P	error covariance

ORCID

Liang Zhang ⬥ https://orcid.org/0000-0001-7109-9130

Shunli Wang ⬥ https://orcid.org/0000-0003-0485-8082

REFERENCES

1. Xu XM, Wu D, Yang L, Zhang H, Liu GJ. State estimation of lithium batteries for energy storage based on dual extended Kalman filter. *Math Probl Eng*. 2020;2020(1):1-11.

2. Niri MF, Bui TMN, Dinh TQ, Hosseinzadeh E, Yu TF, Marco J. Remaining energy estimation for lithium-ion batteries via Gaussian mixture and Markov models for future load prediction. *J Energy Storage*. 2020;28(1):1-27.

3. Chang JQ, Chi MS, Shen T. Model based state-of-energy estimation for LiFePO4 batteries using unscented particle filter. *J Power Electron*. 2020;20(2):624-633.

4. Meng JH, Stroe DI, Ricco M, Luo GZ, Teodorescu R. A simplified mode based state-of-charge estimation approach for lithium-ion battery with dynamic linear model. *IEEE Trans Ind Electron*. 2019;66(10):7717-7727.

5. Chen YY, Yang ZL, Wang YB. SOC estimation of lead carbon batteries based on the operating conditions of an energy storage system in a microgrid system. *Energies*. 2020;13(1):1-25.

6. Li PH, Zhang ZJ, Xiong QY, et al. State-of-health estimation and remaining useful life prediction for the lithium-ion battery based on a variant long short term memory neural network. *J Power Sources*. 2020;459(228069):1-12.

7. Shu X, Li G, Shen JW, et al. An adaptive fusion estimation algorithm for state of charge of lithium-ion batteries considering wide operating temperature and degradation. *J Power Sources*. 2020; 462(1):1-13.

8. Ma ZY, Yang RX, Wang ZP. A novel data-model fusion state- of-health estimation approach for lithium-ion batteries. *Appl Energy*. 2019;237:836-847.

9. Xu YD, Hu MH, Zhou AJ, et al. State of charge estimation for lithium-ion batteries based on adaptive dual Kalman filter. *App Math Model*. 2020;77:1255-1272.

10. Li HH, Wang XY, Saini A, Zhu YQ, Wang YP. State of charge estimation for lithium-ion battery models based on a thermo- electric coupling model. *Int J Electrochem Sci*. 2020;15(5):3807- 3824.

11. Li LL, Liu ZF, Wang CH. The open-circuit voltage characteristic and state of charge estimation for lithium-ion batteries based on an improved estimation algorithm. *J Test Eval*. 2020; 48(2):1712-1730.

12. Chen Z, Xiao JP, Shu X, Shen SQ, Shen JW, Liu YG. Model- based adaptive joint estimation of the state of charge and capacity for lithium-ion batteries in their entire lifespan. *Energies*. 2020;13(6):1-15.

13. Chen ZW, Yang LW, Zhao XB, Wang YR, He ZJ. Online state of charge estimation of Li-ion battery based on an improved unscented Kalman filter approach. *App Math Model*. 2019;70: 532-544.

14. Yang, L, Cai YS, Yang YX, Deng ZW. Supervisory long-term prediction of state of available power for lithium-ion batteries in electric vehicles. *Appl Energy*. 2020; 257(1):1-18.

15. Tan XJ, Tan YQ, Zhan D, et al. Real-time state-of-health estimation of lithium-ion batteries based on the equivalent internal resistance. *IEEE Access*. 2020;8:56811-56822.

16. Zhang D, Dey S, Perez HE, Moura SJ. Real-time capacity estimation of lithium-ion batteries utilizing thermal dynamics. *IEEE Trans Control Syst Technol*. 2020;28(3):992-1000.

17. Chen L, Chen J, Wang HM, et al. A novel remaining useful life prediction framework for lithium-ion battery using grey model and particle filtering. *Int J Energy Res*. 2020;44(9):7435-7449.

18. Xiong R, Yang RX, Chen ZY, Shen WX, Sun FC. Online fault diagnosis of external short circuit for lithium-ion battery pack. *IEEE Trans Ind Electron*. 2020;67(2):1081-1091.

19. Liu ZF, Ivanco A, Onori S. Aging characterization and modeling of nickel-manganese-cobalt lithium-ion batteries for 48V mild hybrid electric vehicle applications. *J Energy Storage*. 2019;21:519-527.

20. He YL, He R, Guo B, et al. Modeling of dynamic hysteresis characters for the lithium-ion battery. *J Electrochem Soc*. 2020; 167(9):1-14.

21. Zhang SZ, Guo X, Zhang XW. A novel one-way transmitted co- estimation framework for capacity and state-of-charge of lithium-ion battery based on double adaptive extended Kalman filters. *J Energy Storage*. 2021;33(1):1-16.

22. Shi Y, Ahmad S, Tong Q, et al. The optimization of state of charge and state of health estimation for lithium-ions battery using combined deep learning and Kalman filter methods. *Int J Energy Res*. 2021;45(7):11206-11230.

23. Zhang Q, Cui NX, Li Y, Duan B, Zhang CH. Fractional calculus based modeling of open circuit voltage of lithium-ion batteries for electric vehicles. *J Energy Storage*. 2020;27(1):1-8.

24. Safdari M, Sadeghzadeh S, Ahmadi R. Tailoring the life cycle of lithium-ion batteries with a passive cooling system: a comprehensive dynamic model. *Int J Energy Res*. 2021;45(5):7884-7902.

25. Ren Z, Du CQ, Wu ZY, Shao JB, Deng WJ. A comparative study of the influence of different open circuit voltage tests on model- based state of charge estimation for lithium-ion batteries. *Int J Energy Res*. 2021;1(1):1-20.

26. Miao H, Du CQ, Wu ZY, Shao JB, Deng WJ. A novel online model parameters identification method with anti-interference characteristics for lithium-ion batteries. *Int J Energy Res*. 2021; 45(6):9502-9517.

27. Xiong R, Chen JJ, Mao L, Qu KQ, Zhao JB, Zhu YJ. A set membership theory based parameter and state of charge co-estimation method for all-climate batteries. *J Clean Prod*. 2020;249(1): 1-16.

28. Xie Y, Li LL, Yu QQ, Jin Q, Yang RX. Novel mesoscale electro-thermal modeling for lithium-ion batteries. *IEEE Trans Power Electron*.

2020;35(3):2595-2614.

29. Wang YJ, Li W, Hu XS, Zou CF, Feng F, Tang XL. A fractional- order model-based state estimation approach for lithium-ion battery and ultra-capacitor hybrid power source system considering load trajectory. *J Power Sources*. 2020;449(1):1-12.

30. Xu W, Xu JL, Yan XF. Lithium-ion battery state of charge and parameters joint estimation using cubature Kalman filter and particle filter. *J Power Electron*. 2020;20(1):292-307.

31. Xu JN, Xu JL, Yan XF. Parameter identification of electrolyte decomposition state in lithium-ion batteries based on a reduced pseudo two-dimensional model with Pade approximation. *J Power Sources*. 2020;460(1):1-11.

32. Ungurean L, Micea MV, Carstoiu G. Online state of health prediction method for lithium-ion batteries, based on gated recurrent unit neural networks. *Int J Energy Res*. 2020;44(8):6767- 6777.

33. Tian Y, Lai RC, Li XY, Xiang LJ, Tian JD. A combined method for state-of-charge estimation for lithium-ion batteries using a long short-term memory network and an adaptive cubature Kalman filter. *Appl Energy*. 2020;265(1):1-14.

34. Tian JP, Xiong R, Shen WX, Wang J, Yang RX. Online simultaneous identification of parameters and order of a fractional order battery model. *J Clean Prod*. 2020;247(1):1-13.

35. Schroer P, van Faassen H, Nemeth T, Kuipers M, Sauer DU. Challenges in modeling high power lithium titanate oxide cells in battery management systems. *J Energy Storage*. 2020;28(1): 1-15.

36. Maheshwari A, Paterakis NG, Santarelli M, Gibescu M. Optimizing the operation of energy storage using a non-linear lithium- ion battery degradation model. *Appl Energy*. 2020;261(1):1-10.

37. Liu XT, Paterakis NG, Santarelli M, Gibescu M. An improved state of charge and state of power estimation method based on genetic particle filter for Lithium-ion batteries. *Energies*. 2020; 13(2):1-16.

38. Liu KL, Li Y, Hu XS, Lucu M, Widanage WD. Gaussian process regression with automatic relevance determination kernel for calendar aging prediction of lithium-ion batteries. *IEEE Trans Ind Inform*. 2020;16(6):3767-3777.

39. Li YG, Chen JQ, Lan FC. Enhanced online model identification and state of charge estimation for lithium-ion battery under noise corrupted measurements by bias compensation recursive least squares. *J Power Sources*. 2020;456(1):1-15.

40. Li JH, Liu MS. State-of-charge estimation of lithium-ion batteries using composite multi-dimensional features and a neural network. *IET Power Electron*. 2019;12(6):1470-1478.

41. Wang YJ, Sun ZD, Chen ZH. Development of energy management system based on a rule-based power distribution strategy for hybrid power sources. *Energy*. 2019;175:1055-1066.

42. Xiong R, Tian JP, Shen WX, Sun FC. A novel fractional order model for state of charge estimation in lithium ion batteries. *IEEE Trans Vehic Technol*. 2019;68(5):4130-4139.

43. Song YC, Liu DT, Liao HT, Peng Y. A hybrid statistical data- driven method for on-line joint state estimation of lithium-ion batteries. *Appl Energy*. 2020;261(1):1-13.

44. Li JB, Ye M, Gao KP, Xu XX, Wei M, Jiao SJ. Joint estimation of state of charge and state of health for lithium-ion battery based on dual adaptive extended Kalman filter. *Int J Energy Res*. 2021;1(1):1-16.

45. Lee C, Jo S, Kwon D, Pecht MG. Capacity-fading behavior analysis for early detection of unhealthy Li-ion batteries. *IEEE Trans Ind Electron*. 2021;68(3):2659-2666.

46. Chen ZH, Sun H, Dong GZ, Wei JW, Wu J. Particle filter-based state-of-charge estimation and remaining-dischargeable-time prediction method for lithium-ion batteries. *J Power Sources*. 2019;414:158-166.

47. Wang SL, Stroe DI, Fernandez C, Xiong LY, Fan YC, Cao W. A novel power state evaluation method for the lithium battery packs based on the improved external measurable parameter coupling model. *J Clean Prod*. 2020;242(118506): 1-13.

48. Chen Y, Li CL, Chen SZ, Ren HB, Gao ZP. A combined robust approach based on auto-regressive long short-term memory network and moving horizon estimation for state-of-charge estimation of lithium-ion batteries. *Int J Energy Res*. 2021;1(1): 1-16.

49. Lotfi F, Ziapour S, Faraji F, Taghirad HD. A switched SDRE filter for state of charge estimation of lithium-ion batteries. *Int J Electric Power Energy Syst*. 2020;117(1):1-10..

50. Zhou SD, Liu XH, Hua Y, Zhou XN, Yang SC. Adaptive model parameter identification for lithium-ion batteries based on improved coupling hybrid adaptive particle swarm optimization- simulated annealing method. *J Power Sources*. 2021;482(1):1-13.

51. Zheng YJ, Shi ZH, Guo DX, Dai HF, Han XB. A simplification of the time-domain equivalent circuit model for lithium-ion batteries based on low-frequency electrochemical impedance spectra. *J Power Sources*. 2021;489(1):1-12.

52. Zhang SZ, Zhang XW. A multi time-scale framework for state- of-charge and capacity estimation of lithium-ion battery under optimal operating temperature range. *J Energy Storage*. 2021;35 (1):1-16.